Veröffentlichung

Autoren

Burnazzi, Marco;Radespiel, Rolf

Titel

Design of a Droopnose Configuration for a Coanda Active Flap Application

Publisher o. Konferenz

51th AIAA Aerospace Sciences Meeting including the New Horizons Forum and Aerospace Exposition, Dallas (TX), AIAA 2013-0487

Jahr

2013

Internet-Link (Doi-Nr.)

Design of a Droopnose Configuration for a Coanda Active Flap Application

Marco Burnazzi* and Rolf Radespiel†

Institute of Fluid Mechanics, Technische Universität Braunschweig, 38108 Braunschweig, Germany

The present study describes the fundamentals of droopnose design for improving the aerodynamics of airfoils with active high-lift using a Coanda flap. Increasing the stall angle of attack and reducing the power required by the high-lift system, are the main objectives. The sensitivities of the investigated geometries are described, as well as the physical phenomena that rule the aerodynamic performance.

Nomenclature

C_μ	Momentum coefficient of the Coanda jet
v_j	Averaged velocity of the jet through the plenum exit section
$\dot{m}_j$	Mass flow of the Coanda jet
ρ_∞	Farfield density
v	Local absolute velocity
v_∞	Farfield velocity
S_{ref}	Reference surface
C_p	Pressure coefficient
α	Angle of attack
α_{stall}	Stall angle of attack
$C_{l_{max}}$	Maximum lift coefficient
$C_{d_{stall}}$	Stall drag coefficient
$C_{m_{stall}}$	Stall pitching moment coefficient
Re	Reynolds number
th_{le}	Thickness factor at the leading edge
δ	Flap deflection
β	Camber line angle at the leading edge, due to a rigid deflection of the nose
γ	Camber line angle at the leading edge, due to a smooth camber increase of the nose
L_n	Nose length
L_f	Flap length
c	Airfoil chord
δ_2	Momentum thickness of the boundary layer
h	Local distance from the wall

$\beta = 30°, \quad \alpha = 5° \; C_\mu = 0.06$

I. Introduction

THE future development of the civil air transport is adversely affected by the limited number of airports for long and medium range aircraft. In a few years the airport infrastructures will not be able to support traffic growth as in the previous decades. On the other hand, many small airports are not in use for commercial transport because of short runways and their proximity to populated areas. These problems

*Research Assistant, Institute of Fluid Mechanics TU-Braunschweig.

†Professor, Head of Institute, Institute of Fluid Mechanics TU-Braunschweig and AIAA Senior Member.

may be solved by using a new class of short to medium range transport aircraft, that represent a competitive alternative to the widely used B737, A320 and similar. These new airplanes need to have STOL capabilities and very low noise emissions, in order to allow operations at many small and close-to-city airports. The high-lift systems of these aircraft are the key to their performance, as they are responsible for the low flight speed capabilities of the aircraft and for their noise emissions as well.

The present work is part of the Collaborative Research Center SFB880 (Sonderforschungsbereich 880) located in Braunschweig, Germany. The Center aims at new technologies, that will satisfy the requirements of above. The Center deals with fundamentals in aeroacoustic, active high-lift technologies and flight dynamics. One particular aim is to improve the aerodynamic efficiency of high-lift Coanda flaps and the recent results in this area are the subject of the present paper. The aerodynamic design work focuses on the shape of the airfoil, based on previous work at the Institute of Fluid Mechanics of the Technische Universität Braunschweig, Germany.[1–3] Primary objective of the present research is the achievement of a very high high-lift capability at low power consumption of the active control means. In particular the following strategies form the base of the current research:

- active circulation control using internally blown flaps: this concept yields large lift gains and it can be adapted to different operation points by flap setting;
- gap-less devices: both the trailing edge and the leading edge devices avoid the use of gaps, because gaps are major causes of airframe noise production.

An important effort is focused on the reduction of the power needed by the blowing system. It is well known that the capability of a mechanical flap to provide flow turning is enhanced by an air jet blown from a slot over the suction side of it. Moreover, the mechanical complexity of the system is reduced with respect to a conventional fowler flap, because the flap rotates around a simple hinge, without the need of creating gaps. Flow separation is avoided by the Coanda effect generated by the jet on the curved surface of the flap, that can thus be deflected of very high angles. Figure 1 shows the DLR F15 airfoil modified with the active Coanda flap.

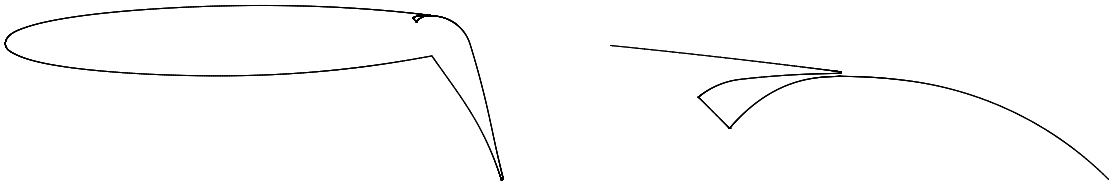

(a) DLR F15 airfoil, modified with active Coanda flap

(b) Detail of the blowing slot

Figure 1: Geometry analyzed and modified in order to evaluate the potentialities of a leading edge device.

The efficiency of the active circulation control device is represented by the lift gain factor, defined as the ratio between the increase of lift coefficient due to the active circulation control system and the jet momentum coefficient needed to obtain this gain. The jet momentum coefficient is given by:

$$C_\mu = \frac{v_j \dot{m}_j}{\frac{1}{2}\rho_\infty v_\infty^2 S_{ref}} \tag{1}$$

In the present paper significant improvements on the airfoil shape to obtain high gain factors are presented. A first part briefly describes the status of Coanda flap design using a fixed geometry of leading edge and wingbox. It appears that very high circulation due to the trailing edge system introduces the need of a leading edge device, in order to avoid local separation starting from the leading edge. Based on the idea of keeping the shape free from gaps, some fixed percentage of the chord length (that is the part of the airfoil not intersected by the wing box) is then modified in order to obtain a droop nose configuration. The new shape is intended for landing and take off operations. Therefore an internal structure, addressed by other teams involved in the SFB880 program, will bring the airfoil back to the clean configuration during cruise conditions. The new shape changes the mean camber line and the thickness. The main design steps that brought out the current most effective configuration are described. As a result, the new shape shows impressing improvements of the blowing efficiency and hence its suitability of application in commercial transport

aircraft. Finally, the stall behavior of the airfoil equipped with the droop nose, and its reaction to different blowing momentum are compared with the ones of the airfoil without any leading edge device. This yields physical insight into the viscous losses in active high-lift systems and into particular stalling mechanisms not known before.

II. Previous studies

PREVIOUS numerical and experimental flow research at Technische Universität Braunschweig resulted in significant experience on active flow control using gapless Coanda flaps. Design sensitivity studies led to the selection of particular flap configurations, and these were thoroughly analyzed in Refs. 1-3.

The most important design parameters are flap deflection angle, momentum coefficient and blowing slot height. While flap angle and blowing momentum coefficient should increase for increased lift targets, optimal slot heights are rather low, with values of around 0.0006 airfoil chord lengths, and mostly independent of the flap angle. The curvature value of the Coanda surface used as flap knuckle shape was less important. Values around 0.07 chord lengths are a reasonable choice. Also flap length suited to achieve high lift gains could be identified. Good values are 0.25 - 0.30 of airfoil chord. With these design choices and assuming steady jet wall blowing, typical lift gains over blowing momentum (blowing gain factor) of 80 were obtained at a lift coefficient around 4 whereas this value was reduced to 55 at a lift coefficient around 6. Similar to other published results on Coanda flaps it was noticed that the angle of attack of maximum lift reduces significantly at higher blowing rates, as seen in figure 2. This indicates that viscous losses due to the suction peak at the nose grow rapidly with alpha. Local blowing at the nose or at other locations of the airfoil did not help much, as it decreased merely the blowing gain factor. Note that leading edge separation occurred for lift coefficients above 6. Blowing from carefully designed slot at the leading edge was not efficient for these extreme cases since it usually decreased overall blowing gain factor also.

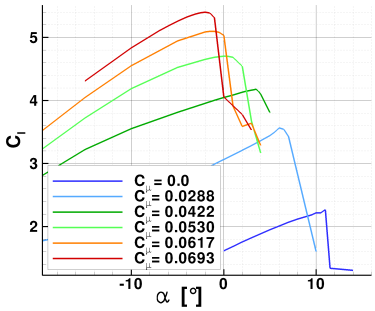

Figure 2: Effect of the blown jet on the stall angle of attack, flap deflection $\delta = 65°$.[10]

The present work aims at solving the observed problems that could prevent Coanda flap configurations from being employed for practical applications. In particular, the main goals are:

- further reduction of the power required by the high-lift device, that is reduction of C_μ ;
- increase of the stall angle of attack, to values suitable for real applications on aircraft.

III. Numerical set-up

THE present droopnose investigations are based on 2D simulations of the DLR F15 airfoil with different nose shapes. The CFD solver employed to perform the analysis is the DLR TAU-Code.[4,5] The Reynolds Averaged Navier-Stockes (RANS) equations are solved by using a finite volume approach. The numerical scheme, turbulence model and parameters have been previously assessed by using wind tunnel experiments.[6,7] In particular the following results and analysis are obtained by a central scheme for the mean flow inviscid flux and a second order upwind Roe scheme for the convective turbulent flux. The turbulence model is Spalart-Allmaras with a correction due to flow rotation and curvature.[8] This last module allows the one-equation turbulence model to maintain a good accuracy also in regions where the streamlines have a high curvature. This characteristic is very important for the simulation of the Coanda phenomenon, which is based on the equilibrium between the inertia forces and the momentum transport in the direction normal to the convex surface.[3]

The space discretization is realized by a dual grid, obtained by the solver from the initial one, as provided by the user. This is performed by connecting the center of each cell and allows to use hybrid meshes. Due to the high amount of simulations required by the present analysis, the number of points has been set by means of a mesh convergence exercise, based on the Richardson extrapolation. This procedure provides an estimation of the space discretization error and allows to obtain the minimum number of points that still gives results with an acceptable accuracy. The resulting grid is made by about 240000 points and composed

by an unstructured grid region and a structured area. The structured grid layer starts from the surfaces and is extended to cover the region where the main viscous phenomena occur. It ensures y^+ lower than 1 close to the wall. In the grid plots of Figure 3 one can see some of the main features of the mesh. An important characteristic of the grid, that makes it suitable for high-lift simulations, is the density of points along the pressure side, as the stagnation point will be situated in this region, and can move quite far from the leading edge. Therefore a high amount of points is necessary to properly capture the flow attachment. The structured region is extended over a large area over the flap, in order to accurately capture vortices expected in case of flow separation from the flap. Both the trailing edge and the edge of the slot lip are discretized by means of a C-block topology, in order to avoid the propagation of high point density in areas where grid points are not needed and could slow down the convergence.

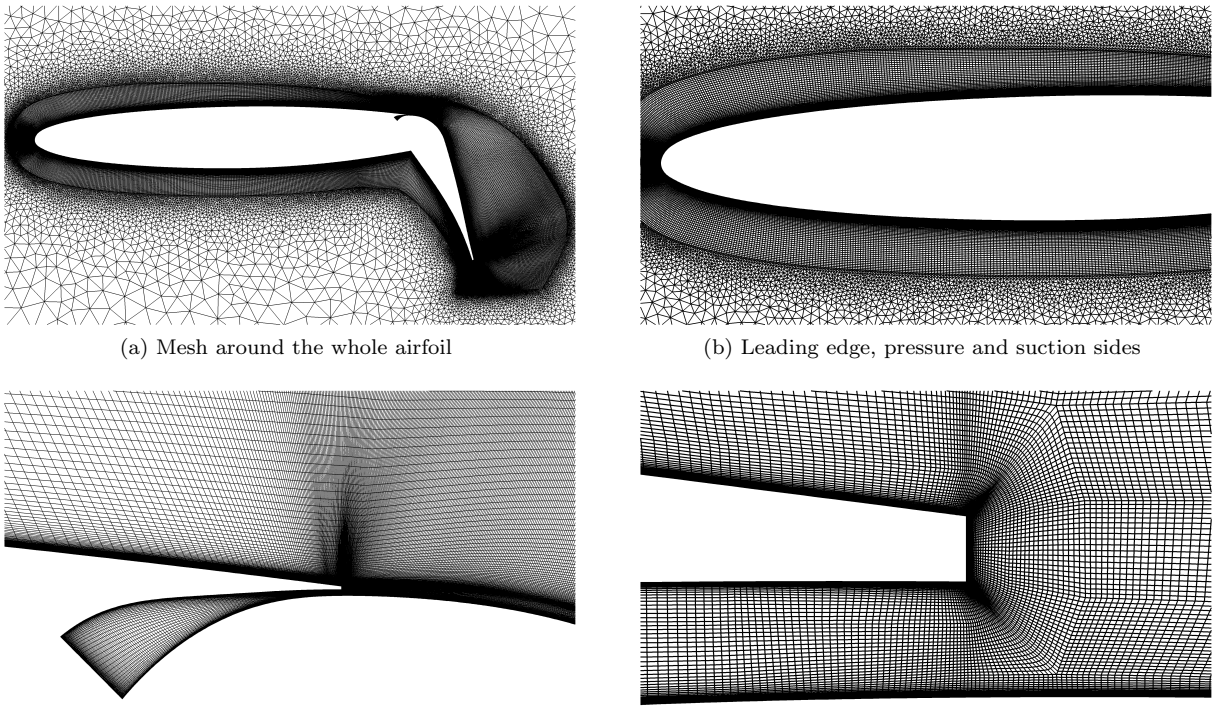

(a) Mesh around the whole airfoil

(b) Leading edge, pressure and suction sides

(c) Plenum and jet exit slot

(d) C-block topology at the plenum exit section

Figure 3: Numerical hybrid grid used for the analysis.

IV. Evolution of the geometry

The modification of the leading edge shape is performed by a python script. This allows to easily integrate the tool in an optimization algorithm. Geometrical leading edge parameters have been chosen in order to have enough degrees of freedom but also to ensure a low number of parameters for the optimization process. An important requirement, coming from nose structure considerations, is the skin length of the modified surface, that has to be equal to the length of the original airfoil. The search for an effective shape begins with the simple deflection of the fixed nose shape, followed by an increase of its thickness and a progressive increase of the mean line camber. The different geometries are evaluated and compared by computing the maximum lift coefficient and the respective angle of attack. In this first step of the analysis the Reynolds number, the blowing energy, the flap deflection angle and the flap length are kept constant : $Re = 10^7$, $C_\mu = 0.06$, $\delta = 65°$, $L_f/c = 0.25$. The allowed length of the droopnose is fixed to $L_n/c = 0.20$.

A. Rigid droopnose

A first simple leading edge device is obtained by deflecting the leading edge downward, without changing its shape (figure 4a). Therefore, this technique does not involve any structure deformation and can be realized by a simple rotation of the nose around a hinge. Thanks to its efficiency and mechanical simplicity, this

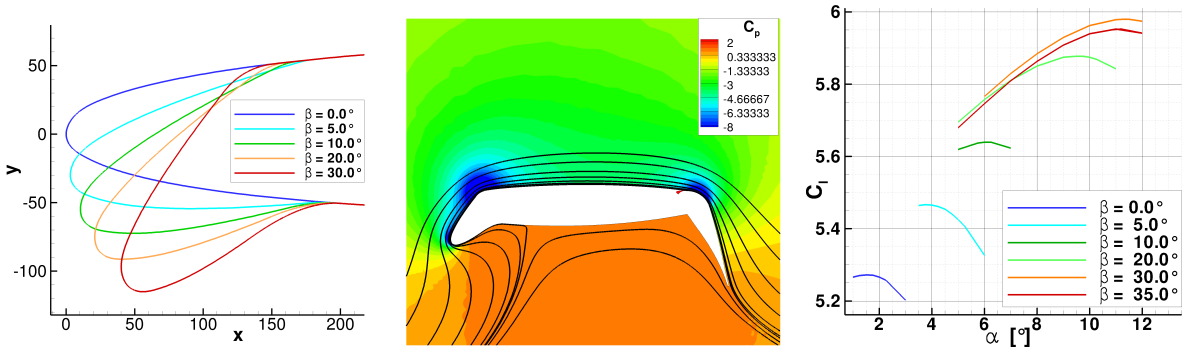

(a) Shapes of rigid droopnose (b) C_p field for $\beta = 30°, \alpha = 5°$ (c) $C_l(\alpha)$ performance increase

Figure 4: Rigid droopnose shapes and behavior

device is currently employed by some of the current commercial transport aircraft, like the Airbus A380.

This configuration is characterized by two strong peaks of low pressure (figure 4b), as the deflection of the nose creates a new region of high curvature on the suction side. Nevertheless, the improvement of lift generation with respect to the clean nose configuration is important, as shown in table 1 and figure 4c, where the deflection is expressed by the angle β. Note that the improvements in lift and angle of attack range are larger than those known from applications in combination with mechanical high-lift flaps.[9]

	$C_{l_{max}}$	$\alpha_{stall}[°]$
Clean nose	5.27	1.5
Droopnose $\beta = 30°$	5.98	11.3

Table 1: Improvements achieved by a rigid rotation of the nose.

B. Thickness increase

In order to reduce the low pressure peaks on the suction side, the thickness of the nose is varied. The new nose contour is obtained by multiplying the distance of each point from the camber line by a function f such that, in the connection to the wingbox (fixed part of the airfoil), is:

$$f(x_{wingbox}) = 1 \tag{2}$$

$$f'(x_{wingbox}) = 0 \tag{3}$$

A parabolic function can be used for the function f, as well as combinations of spline or trigonometric functions. The resulting thickness increase is symmetric with respect to the camber line.

According to figure 5a, the new thickness in a generic point is given by:

$$d_{new} = \bar{d} \cdot f(\bar{x}) \tag{4}$$

In the example the thickness has been increased by a parabolic function, taking as reference parameter the value of the function at the leading edge, th_{le}. Starting from an undeformed nose deflection of 10°, the achievements shown in the table 2 have been reached, thanks to $th_{le} = 1.6$.

	$C_{l_{max}}$	$\alpha_{stall}[°]$
Droopnose $\beta = 10°$, $th_{le} = 1.0$	5.64	6.3
Droopnose $\beta = 10°$, $th_{le} = 1.6$	5.86	9.0

Table 2: Improvements achieved by increasing the thickness of a nose deflected of 10°.

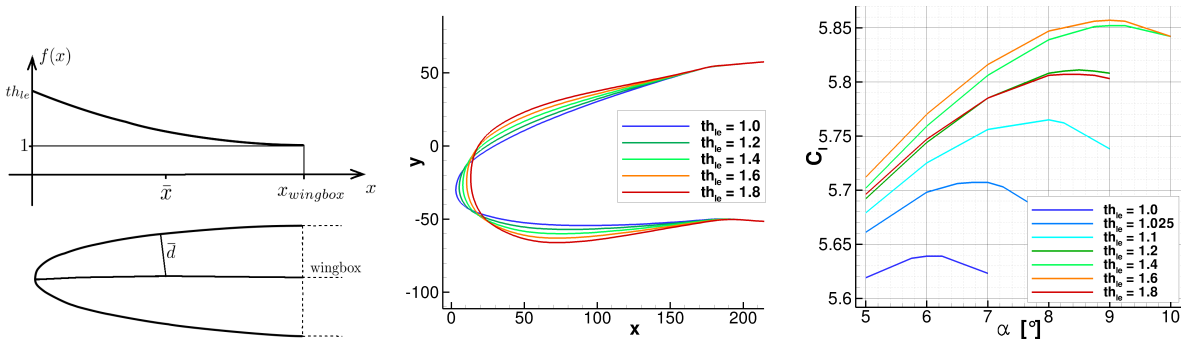

(a) Thickness increasing method (b) Shapes of rigid droopnose with incresed thickness (c) $C_l(\alpha)$ performance increase

Figure 5: Thickness increase, shapes and performances

The thickness increase distributes the low pressure peak over a larger area and reduces the peak value. Nevertheless, a too high value of function f at the leading edge creates an undesired augmentation of the surface curvature, resulting in lower performances (figure 5c).

C. Camber increase

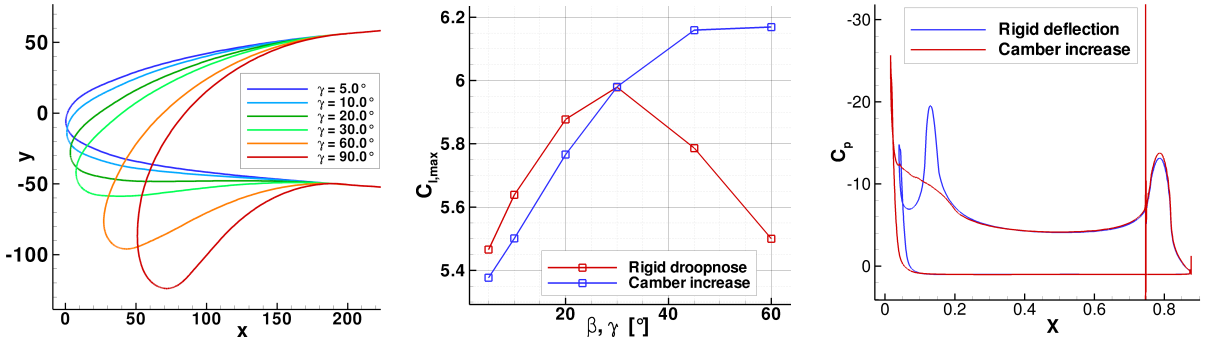

(a) Shapes obtained by camber increase (b) Comparison based on maximum lift coefficient and leading edge angle (c) Pressure coefficient flow fields for equal leading edge angles: $\beta = \gamma = 30°$, $\alpha = 5°$, $C_\mu = 0.06$

Figure 6: Shapes of camber-increased noses and performance comparison to rigid droopnose

A better control of the pressure distribution along the nose is obtained by changing the camber of the mean line. The new camber is controlled by 3 radii of camber curvature: at the wing box, at the leading edge, and at a point in between them. The direct comparison between a rigid nose deflection and a smooth camber increase (figure 6) shows that the low pressure peak at the knee over the flap hinge of the rigid nose does not occur for a smooth camber line, as shown in figure 6c. In particular, for high nose deflections the hinge peak causes very high losses, which bring a strong decrease of performance, see figure 6b. The best result obtained by camber increase, without any thickness variation and using the same value for the three radii, involves the gain shown in table 3.

	$C_{l_{max}}$	$\alpha_{stall}[°]$
Clean nose	5.27	1.5
Droopnose $\gamma = 90°$	6.267	15.0

Table 3: Improvements achieved by increasing the camber of the mean line to an angle at the leading edge of 60°.

D. Camber and thickness increase

The current most effective configuration has been obtained by using both the thickness and the camber increase. In this state of the work, the same value has been given to the three radii of the camber control, that means that the camber line is a circle arc. Very recent studies, aimed at further optimizing the nose shape, have shown some potentials of using a higher curvature in the region of the leading edge and a lower one close to the wingbox. In figure 7 one can see a direct comparison between the clean nose configuration and the currently best one. Both C_p distributions refer to the stall conditions, and result in the coefficients shown in table 4. From the C_p distributions one can see that the low pressure area has been distributed over a wider surface, and the peak of its minimum value has been strongly reduced. This new load distribution results in different stall behaviors, as explained in the following sections. Flow fields of these two results are shown in figures 14e and 17e.

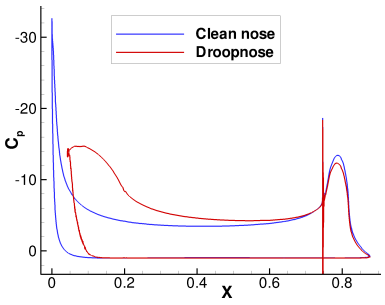

Figure 7: C_p distributions at stall conditions

	$C_{l_{max}}$	$\alpha_{stall}[^\circ]$	$C_{d_{stall}}$	$C_{m_{stall}}$
Clean nose	5.27	1.5	0.0886	-2.184
Droopnose	6.30	15.0	0.107	-2.44
	+19.5%	+13.5	+20.8%	-11.7%

Table 4: Improvements achieved by increasing the camber and the thickness of the nose.

V. Droopnose and clean nose response to variations of C_μ and α

In this section, the two geometries of section IV.D are analyzed for different blowing momentum, and their behavior at high angles of attack is described. As shown above, the droopnose has a very strong effect on increasing both the maximum lift coefficient and the stall angle of attack. Moreover, the phenomena that generate stall are different with respect to the clean configuration. It is worth to investigate the most important flow quantities that govern the flow around the airfoil, and their interaction.

As shown in figure 8a the position of the jet is determined by two opposing effects. On one side the jet is kept attached to the flap surface by the Coanda effect. On the other side the inertia of the outer flow, that comes from the leading edge over the suction side of the airfoil, causes slowing down of the jet and possibly separation from the wall. One can consider the magnitude of these two effects as dependent on the following factors:

C_μ The momentum coefficient of the jet affects both the Coanda effect and the mixing between the jet and the outer flow. In the following it is explained how these two effects are balanced, in relation to the nose shape, the angle of attack, and C_μ itself.

δ_2 **over the slot** The momentum thickness of the boundary layer over the slot describes the state of the outer flow as it is mixed with the jet. The value of the momentum thickness in this point depends on the pressure gradient along the suction side of the airfoil, which is affected by the angle of attack, the nose shape, and the jet momentum coefficient.

α Downstream of the slot the outer flow receives from the jet the momentum needed to flow along the flap in presence of a positive pressure gradient, which is determined by the angle of attack.

The reaction of the flow field to variations of C_μ and α is described in the following sections by means of boundary layer velocity profiles and thicknesses, calculated in two significant locations: over the slot, and close to the trailing edge (Figure 8b).

In figure 9a one can see the momentum thickness of the boundary layer when the jet reaches the trailing edge. An increase of jet momentum coefficient improves the Coanda effect, which keeps the jet closer to

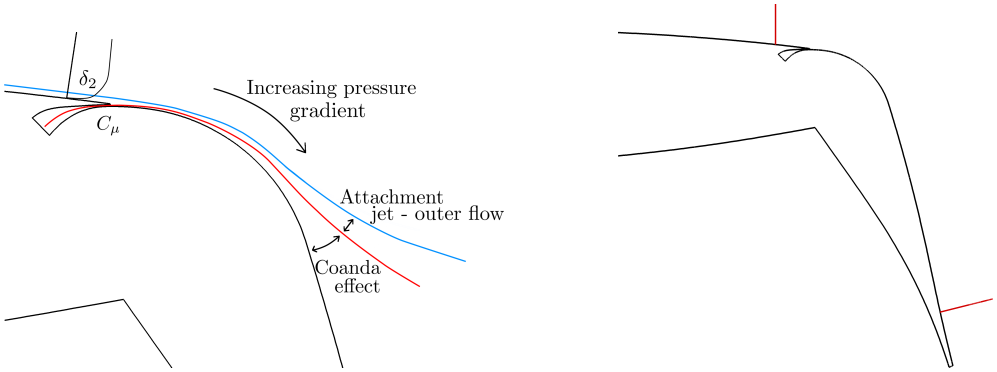

(a) Working principle scheme of the Coanda flap

(b) Locations where the boundary layer is analyzed

Figure 8: References for the flow field analysis

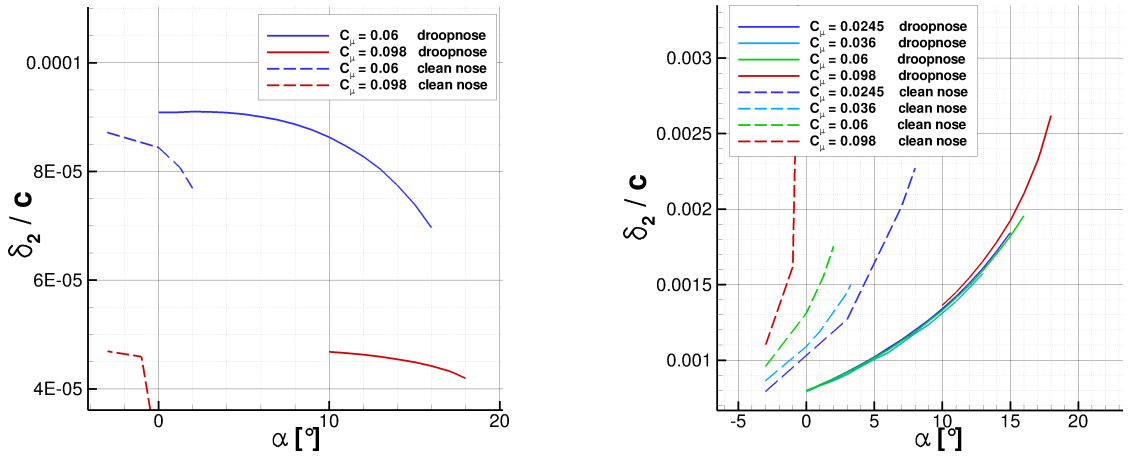

(a) δ_2 of the boundary layer at the trailing edge

(b) δ_2 of the boundary layer over the slot

Figure 9: Momentum thickness of the boundary layer in the two locations, for different C_μ and α

the wall reducing the boundary layer momentum thickness at the trailing edge. An increase of α involves a higher positive pressure gradient, as well as higher losses at the leading edge. As a result of these two factors a progressive separation occurs between outer flow and jet, which allows the jet to flow closer to the wall. In the following, examples of this phenomenon are presented.

In this scenario the shape of the nose is of primary importance. In fact, it determines the state of the outer flow when it reaches the jet. Figures 10a and 10b show how the velocity profile of the boundary layer over the slot is affected by the C_μ. In both cases a higher blowing ratio creates a higher edge velocity. However, with clean nose, the boundary layer becomes thicker, whereas the thickness remains mostly constant with droopnose. Figure 9b shows the momentum thickness of the boundary layer in this area. With both geometries, the angle of attack has a strong influence on the boundary layer. The clean nose configuration is much more sensitive to jet momentum variation. This last point plays a key role in the stall behavior of the two configurations, as explained in the following.

A. Stall performances

Thanks to the considerations mentioned above, it is possible to explain the different stall behaviors of the two leading edge configurations. Figure 11 shows the responses to different jet momentum, in terms of maximum lift coefficient and stall angle of attack.

$C_{l_{max}}$ vs C_μ In figure 11a the increasing jet momentum involves an augmentation of circulation, which

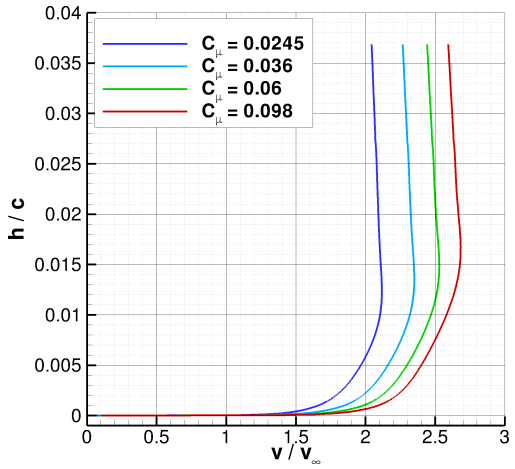

(a) Clean nose, $\alpha = -3°$

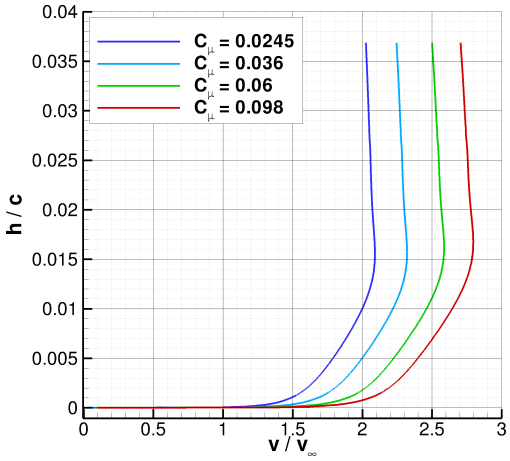

(b) Droopnose, $\alpha = 10°$

Figure 10: Velocity profiles over the jet slot, at constant angles of attack

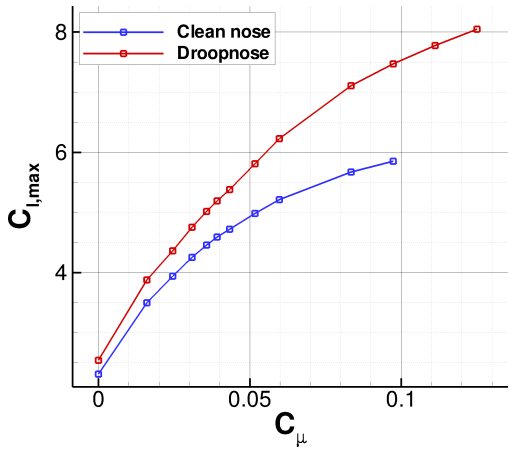

(a) Effect of the C_μ on the maximum lift coefficient

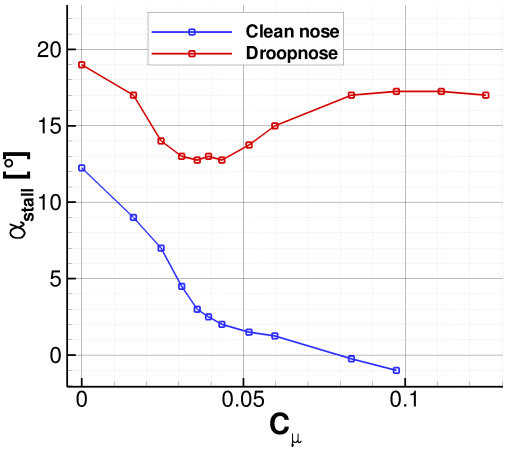

(b) Effect of the C_μ on the stall angle of attack

Figure 11: Response of the two airfoils to different momentum coefficients, $\delta = 65°$.

results in higher C_l. However, the efficiency of blowing decreases at high C_μ. For low momentum, the graph has a higher slope, and describes the regime of "boundary layer control." In these conditions C_μ is not sufficient to keep the outer flow attached until the trailing edge, causing the jet to separate from the wall. An increasing C_μ delays the separation point, until the trailing edge is reached. In this condition a second regime begins: "supercirculation." The increase of C_l is given by a further deflection of the streamlines due to the jet effect after the trailing edge. This explains the lower efficiency of this second region: in order to obtain the same improvement of C_l, a higher increase of blowing power is needed.

α_{stall} vs C_μ The stall angle of attack directly depends on the interaction between the flow dynamics at the leading edge and at the flap. In fact, as mentioned above, a very effective trailing edge device causes a strong peak of low pressure at the leading edge, that can involve a leading edge separation. This can be avoided by leading edge protection, which, in the present case, creates a different stall mechanism. This explains the different trends shown in figure 11b. As the $C_{l_{max}}$ also the stall angle of attack is sensitive to the different regimes: boundary layer control and supercirculation. A more detailed discussion about the stalling behaviors is presented in the next sections.

Note that the values corresponding to the no-blowing conditions, are considered less accurate than the other cases, because of the large separation area that occurs behind the 65°-deflected flap. These regions are characterized by unsteady phenomena and vortices, which cannot be accurately captured with an almost

steady Spalart-Allmaras simulation.

B. Stall behavior in boundary layer control regime

In this regime the jet does not have sufficient momentum to keep the outer flow attached to the flap surface until the trailing edge. At low angles of attack the jet separates from the wall following the same path as the outer flow (figures 14a, 17a, 17b). As the angle of attack increases both the positive pressure gradient over the flap and the losses at the leading edge increase. The result of these effects is described in figure 12, which shows the velocity profile just before the separation point, for $C_\mu = 0.036$ in the droopnose configuration. Until $\alpha = 8°$ the positive pressure gradient increases the separation region. Whereas, for higher angles of attack the losses at the leading edge become more important and the attachment between the jet and the outer flow decreases, leaving the jet to flow closer to the surface of the flap. This phenomenon can cause the separation to disappear. In some cases a recirculation area occurs between the jet and the outer flow. This happens typically for low blowing rates: figures 14b, 14c, 17c. However, the very high losses at the leading edge caused by high C_μ in the clean nose configuration, can cause a similar flow topology, as shown in figure 14i.

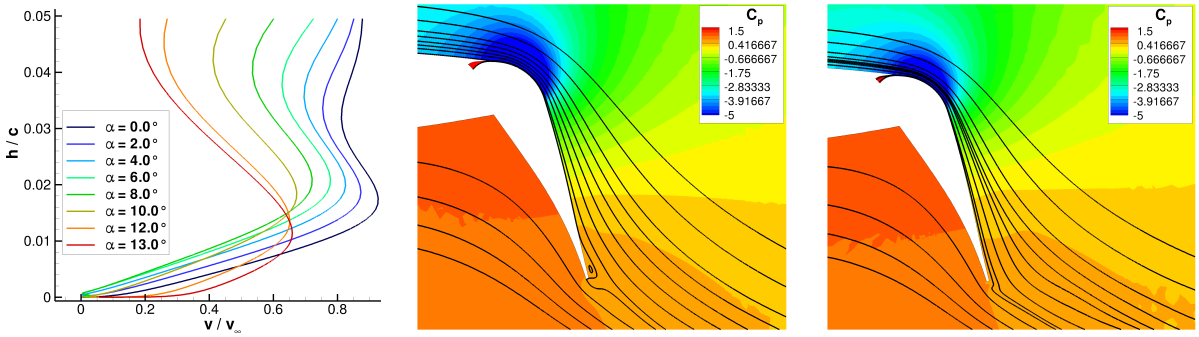

(a) Velocity profiles at $0.05c$ ahead of the trailing edge

(b) $\alpha = 8°$

(c) $\alpha = 13°$

Figure 12: Trailing edge boudary layer evolution, for $C_\mu = 0.036$, droopnose

An increase of C_μ improves both the Coanda effect and the momentum transferred to the outer flow. As a result the separation point is moved toward the trailing edge. This increases the lift coefficient, but decreases the stall angle of attack. In more detail, since the separation occurs closer to the trailing edge, the local positive pressure gradient is more sensitive to α. Therefore the progressive separation between the jet and the outer flow begins earlier.

C. Stall behavior in supercirculation regime

With respect to the boundary layer control regime, now the jet has sufficient momentum to flow always attached to the flap surface. Therefore the position of the jet remains constant, contrarily to the previous case. In this condition the condition at the leading edge plays a more important role. Stall happens because of decambering of the outer flow. A larger α increases the losses at the leading edge and the positive pressure gradient over the flap, which reduce the attachment between jet and outer flow (figure 9a).

As mentioned above, the losses caused by high C_μ at the leading edge are quite important in the clean nose geometry, whereas they are almost negligible in the case of droopnose (figures 9,10). This explains the different trends shown in figure 11. With both configurations an increase of C_μ increases the momentum transferred to the outer flow from the jet. However, in the case of clean nose the outer flow loses a large amount of momentum at the leading edge, therefore stall occurs at lower angles of attack. The droopnose does not creates such high losses, therefore the outer flow will overcome higher positive pressure gradients, and stall is delayed. This happens until C_μ reaches values around 0.0834. Note that at 17° for the angle of attack the jet leaves the trailing edge in direction normal to the freestream, just at the maximum of lift.

D. Aerodynamic coefficients

The pressure coefficient distributions shown in figures 15 and 18 describe a progressive loading of the nose and unloading of the Coanda surface for an increasing angle of attack. As a result the negative pitching moment reduces, as one can see in figures 16 and 19. The moment reference point is fixed for both geometries at 0.25 of the clean configuration chord. The absolute value of the pitching moment is significantly lower in the case of droopnose, thanks to the distribution of the leading-edge low pressure over a larger area.

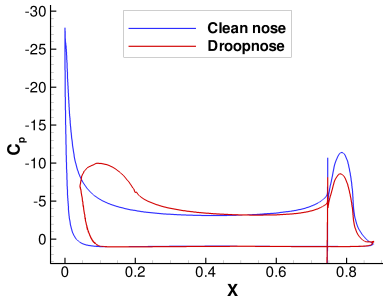

Figure 13: C_p distribution corresponding to $C_l = 4.719$

In figure 13 one can compare the pressure coefficient distributions of the two configurations, corresponding to a same lift coefficient. $C_l = 4.719$, is obtained by the clean configuration with $C_\mu = 0.0433$ at $\alpha = 2.0°$, which is the stall angle of attack. The same C_l is obtained by the droopnose configuration with $C_\mu = 0.0309$ at $\alpha = 12.0°$, which is one degree before stall. The different blowing ratio results in a different load on the Coanda surface, which is much lower for the droopnose case. As a result of the different load distribution, the aerodynamic coefficients are as shown in table 5.

	C_μ	$\alpha[°]$	C_l	C_d	C_m
Clean nose	0.0433	2.0	4.719	0.0719	-0.808
Droopnose	0.0309	12.0	4.719	0.0784	-0.677
	-28.6%	+10.0		+9.0%	+16.2%

Table 5: Aerodynamic coefficients for $C_l = 4.719$

VI. Conclusion

New results on the combination of well designed Coanda flaps and droopnoses are presented. This combination brings a surprisingly large effect of the droopnose that is significantly larger than the effect known with mechanical high-lift flaps. The effect is to reduce the needed blowing power of the Coanda flap and to increase the angle of attack of maximum lift coefficient. A target $C_l \approx 4.7$ can be obtained with about 28% less jet momentum thanks to the droopnose, which increases the lift gain factor of the same proportion. Moreover, the stall angle of attack is brought to values suitable for landing and take off operations: from 2° to 12°. The pitching moment represents an important issue for the stability of the aircraft, and due to an improved load distribution along the chord, and the lower jet momentum, the pitching moment is reduced by about 16%.

The analysis of the stall mechanism highlighted some important, unexpected phenomena, which will play an important role in future developments of the technology. For example, the evolution of the flow features at high angles of attack would be fundamental in the close loop control of the active high-lift system.

However, the presented flow simulations will have to be confirmed by the use of more accurate turbulence models, as well as by using experimental data. Water tunnel experiments are currently being prepared at the Technische Universität Braunschweig, and these tests will employ the droopnose geometry analyzed in the present paper.

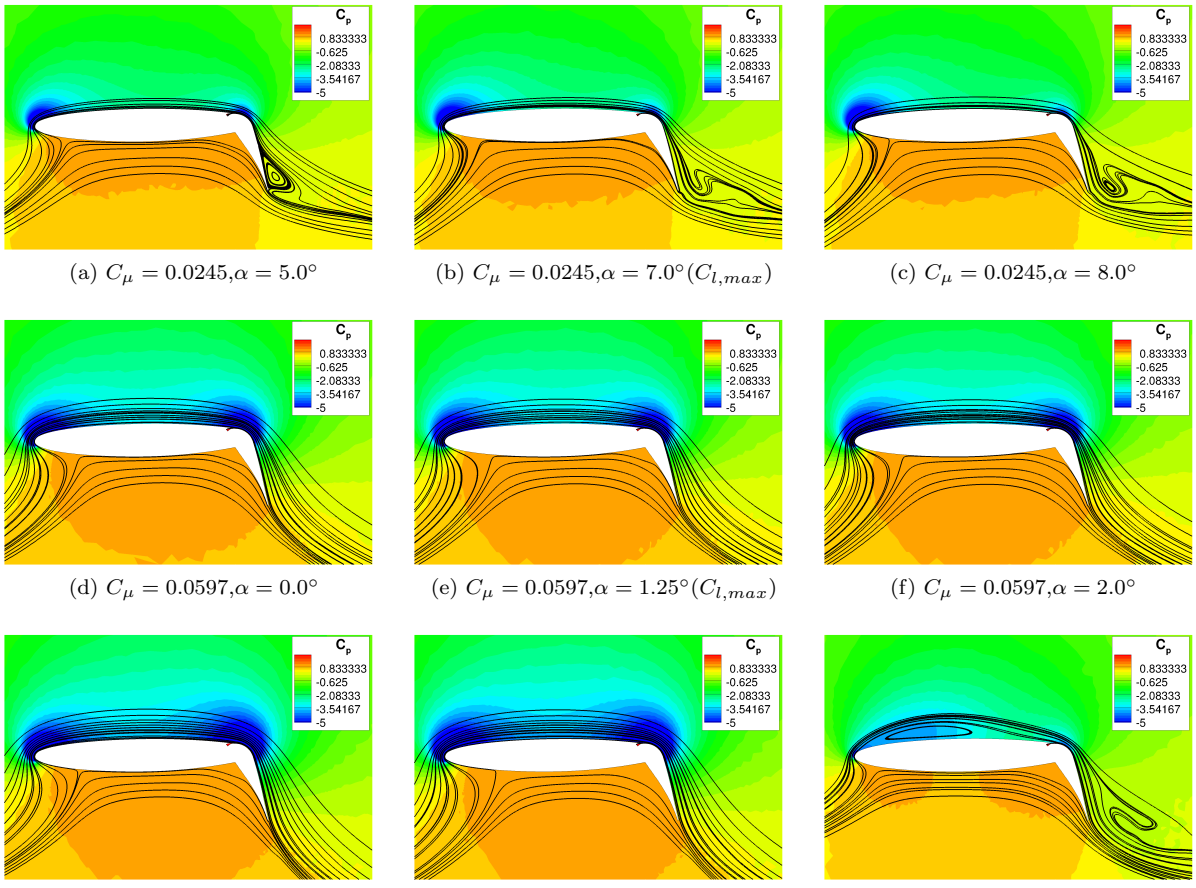

(a) $C_\mu = 0.0245$,$\alpha = 5.0°$ (b) $C_\mu = 0.0245$,$\alpha = 7.0°(C_{l,max})$ (c) $C_\mu = 0.0245$,$\alpha = 8.0°$

(d) $C_\mu = 0.0597$,$\alpha = 0.0°$ (e) $C_\mu = 0.0597$,$\alpha = 1.25°(C_{l,max})$ (f) $C_\mu = 0.0597$,$\alpha = 2.0°$

(g) $C_\mu = 0.0973$,$\alpha = -3.0°$ (h) $C_\mu = 0.0973$,$\alpha = -1.0°(C_{l,max})$ (i) $C_\mu = 0.0973$,$\alpha = 0.0°$

Figure 14: Clean nose configuration, C_p contour and streamlines

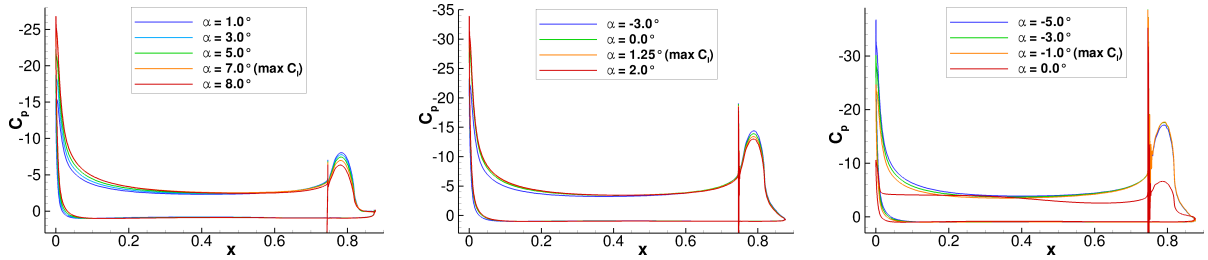

(a) $C_\mu = 0.0245$ (b) $C_\mu = 0.0597$ (c) $C_\mu = 0.0973$

Figure 15: Clean nose configuration, C_p distributions

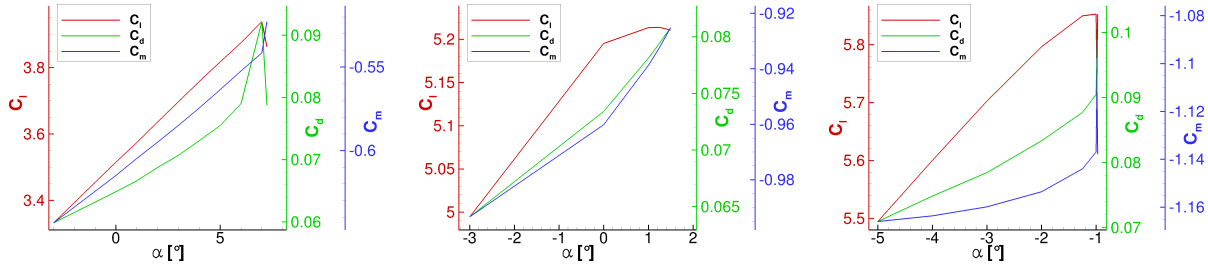

(a) $C_\mu = 0.0245$ (b) $C_\mu = 0.0597$ (c) $C_\mu = 0.0973$

Figure 16: Clean nose configuration, aerodynamic coefficients

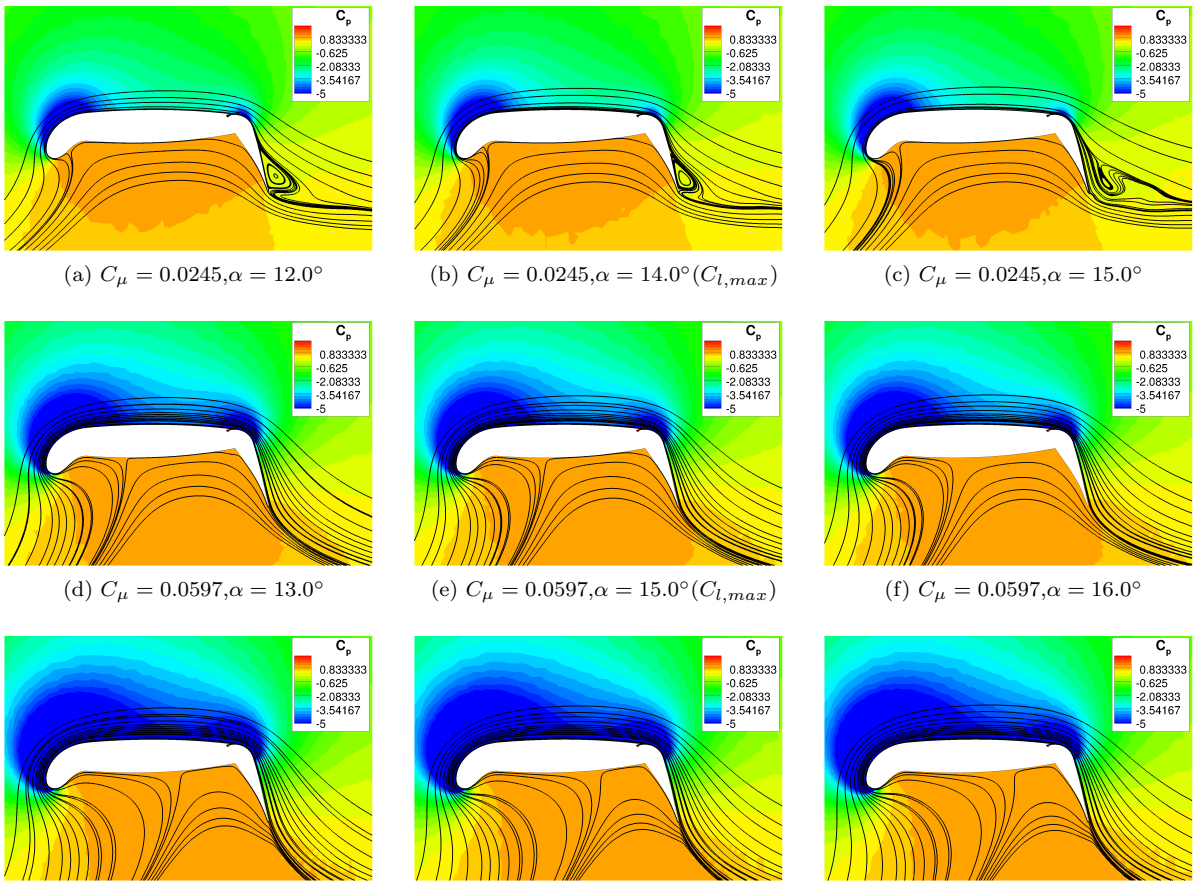

(a) $C_\mu = 0.0245$,$\alpha = 12.0°$ (b) $C_\mu = 0.0245$,$\alpha = 14.0°(C_{l,max})$ (c) $C_\mu = 0.0245$,$\alpha = 15.0°$

(d) $C_\mu = 0.0597$,$\alpha = 13.0°$ (e) $C_\mu = 0.0597$,$\alpha = 15.0°(C_{l,max})$ (f) $C_\mu = 0.0597$,$\alpha = 16.0°$

(g) $C_\mu = 0.0973$,$\alpha = 15.0°$ (h) $C_\mu = 0.0973$,$\alpha = 17.0°(C_{l,max})$ (i) $C_\mu = 0.0973$,$\alpha = 18.0°$

Figure 17: Droopnose configuration, C_p contour and streamlines

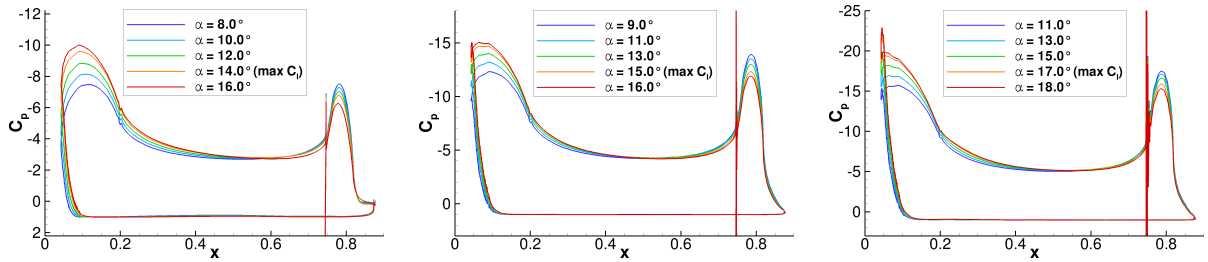

(a) $C_\mu = 0.0245$ (b) $C_\mu = 0.0597$ (c) $C_\mu = 0.0973$

Figure 18: Droopnose configuration, C_p distributions

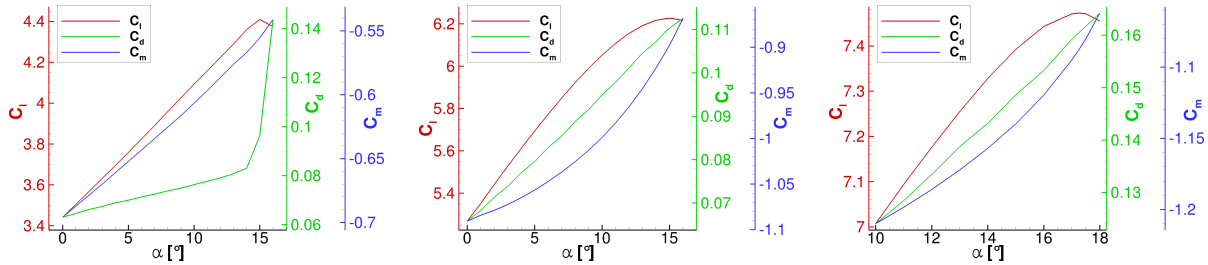

(a) $C_\mu = 0.0245$ (b) $C_\mu = 0.0597$ (c) $C_\mu = 0.0973$

Figure 19: Droopnose configuration, aerodynamic coefficients

References

[1]Jensch, C., Pfingsten, K. C., Radespiel, R., Schuermann, M., Haupt, M., and Bauss, S.: *Design Aspects of a Gapless High-Lift System with Active Blowing*, DLRK 2009, Aachen, 2009.

[2]Jensch, C., Pfingsten, K. C., and Radespiel, R.: *Numerical Investigation of Leading Edge Blowing and Optimization of the Slot and Flap Geometry for a Circulation Control Airfoil*, Notes on Numerical Fluid Mechanics and Multidisciplinary Design, Vol. 112, Springer Verlag, 2010.

[3]Pfingsten, K. C., Jensch, C., Körber, K. V., and Radespiel, R.: *Numerical simulation of the flow around circulation control airfoils*, First CEAS European Air and Space Conference, Berlin, 2007.

[4]Kroll, N., Rossow, C.-C., Schwamborn, D., Becker, K., and Heller, G.: *MEGAFLOW - A Numerical Flow Simulation Tool for Transport Aircraft Design*, ICAS Congress, Toronto, 2002.

[5]Schamborn, D., Gerhold, T., and Heinrich, R., *The DLR TAU-Code: Recent applications in Research and Industry*, ECCOMAS CFD, Egmond aan Zee, The Netherlands, 2006.

[6]Pfingsten, K. C., and Radespiel, R.: *Experimental and numerical investigation of a circulation control airfoil*, 47th AIAA Aerospace Sciences Meeting, Orlando, AIAA 2009-533.

[7]Pfingsten, K. C., Cecora, R. D., and Radespiel, R.: *An experimental investigation of a gapless high-lift system using circulation control*, Katenet II Conference, Bremen, 2009.

[8]Shur, M. L., Strelets, M. K., Travin, A. K., and Spalart, P. R.: *Turbulence Modeling in Rotating and Curved Channels: Assessing the Spalart-Shur Correction*, AIAA Journal, Vol. 38, pp. 784-792, 2000.

[9]Raymer, D. P.: *Aircraft design: a conceptual approach*, AIAA Education Series (1999).

[10]Beck, N., Wentrup, M., and Radespiel, R.: *Realisierung eines Windkanalexperiments für Aktiven Hochauftrieb*, DLRK2011_241373, 2011.